

pubs.acs.org/acscatalysis Research Article

Polarized Ni⁰-Ni⁰⁺ Catalysts Enable Asymmetric C—C Coupling for Long-Chain Hydrocarbons in Electrochemical CO₂ Reduction

Haowen Ding,§ Wenwei Cai,§ Xinzhe Yang, Yu Zhang, Shunning Li,* Feng Pan,* and Shisheng Zheng*



Cite This: ACS Catal. 2025, 15, 9793-9803



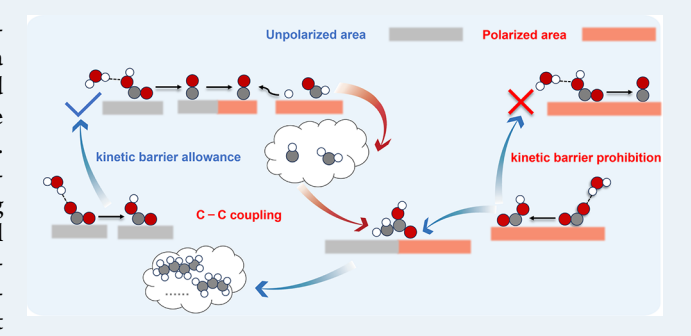
ACCESS

Metrics & More

Article Recommendations

s Supporting Information

ABSTRACT: The efficient electrochemical CO₂ reduction reaction (CO₂RR) to long-chain hydrocarbons (C₃₊) still remains a formidable task even on the widely investigated copper-based catalysts. Recently, nickel-based catalysts have garnered wide attention for their promising ability to generate C₃₊ products. The design of Ni⁰-Ni^{δ +} domains, analogous to the renowned Cu⁰-Cu^{δ +} strategy, stands out as a hallmark approach, achieving substantial yields of C₃–C₆ compounds. However, theoretical understanding remains significantly limited. Here, we employ full-solvent ab initio molecular dynamics simulations with a slow-growth approach to investigate Ni⁰-Ni^{δ +}-mediated C–C coupling at partially polarized nickel. In this system, the nonpolarized region is



constantly covered by the generated *CO, while the polarized domain—through strategic modulation of Ni's d-band center—mitigates the poisoning effects of *CO₂ and *CO, thereby enhancing their activation. This facilitates C–C coupling primarily between *COOH and *CH_x(x = 1, 2), with significantly lower kinetic barriers compared to conventional *CO-involved pathways, laying the foundation for sustained carbon chain growth. Extending this concept to other metals (M = Fe, Rh, Pd, Co and Ru) with similar adsorption characteristics akin to Ni further underscores the potential of M⁰-M^{δ+} domains for CO₂ electroreduction. Our study elucidates the microscopic mechanisms by which polarization strategies promote the formation of long-chain products, providing an original perspective for designing CO₂ electroreduction catalysts.

KEYWORDS: CO₂ electrochemical reduction, asymmetric C-C coupling, long-chain hydrocarbons, nickel-based catalysts, ab initio molecular dynamics

■ INTRODUCTION

The electrochemical reduction of carbon dioxide (CO_2RR) into valuable multicarbon (C_{2+}) products offers a highly promising strategy for closing the carbon cycle while efficiently storing electricity generated from renewable energy sources. ^{1–3} Copper is considered the only metal capable of reducing CO_2 to C_2 products, albeit with relatively low Faradaic efficiency in its pure metallic state. ^{4–6} A major challenge, underscored by extensive experimental and theoretical studies, lies in the C–C coupling process, which is crucial for directing the formation of C_{2+} products, yet is hindered by slow kinetics under ambient conditions. ^{7,8}

Among diverse strategies aimed at addressing this challenge, the construction of localized $\text{Cu}^0\text{-}\text{Cu}^{\delta+}$ environments through methods such as doping, morphology engineering, and molecular modification has emerged as one of the most effective approaches for promoting CO_2 reduction to multicarbon products on copper-based catalysts, garnering sustained interest and extensive research over the past decades. $^{9-19}$ It is widely recognized that Cu^0 and $\text{Cu}^{\delta+}$ sites can increase *CO coverage and, owing to their distinct electron affinities, induce different activation states in neighboring *CO species. 10,13

This facilitates *CO-*CO coupling or enables further reduction of *CO, promoting asymmetric C–C coupling modes, e.g., *CO-*COH^{9,11} or *CO-*CHO.²⁰ Through this strategy, the selectivity of C_2 products, including ethylene and ethanol, on copper-based catalysts has surpassed 80%.¹⁴ However, the efficient production of longer chain carbon products (C_{3+}) still remains a formidable task.

In recent years, Ni-based alloys and compounds have gained significant attention as highly promising CO_2RR systems due to their unparalleled potential for producing C_{3+} hydrocarbons. Intriguingly, the construction of $Ni^0-Ni^{\delta+}$ domain by oxygen doping in pure nickel has also been identified as an effective strategy to facilitate C-C coupling. This imparts the catalyst with a remarkable ability to produce C_3-C_6 products in substantial quantities, akin to the Fischer—

Received: November 28, 2024 Revised: April 29, 2025 Accepted: May 21, 2025 Published: May 27, 2025





Tropsch synthesis in thermochemical processes.²¹ Notably, researchers have observed that cofeeding CO2 and CO as reactant gases yields a greater amount of multicarbon products compared to using either gas individually. This indicates that the carbon species participating in C-C coupling may originate from distinct stages—one prior to the formation of *CO and the other subsequent-marking a significant departure from the classical *CO dimerization mechanism.²¹ Despite the pioneering work, the limited research on the role of Ni^0 - $Ni^{\delta+}$ has so far fallen short of achieving the same level of mechanistic understanding as that of Cu-based counterparts. In particular, the detailed atomic reaction pathway and energetics, as well as the electronic structure origins of performance regulation, arise from the polarized regions. Additionally, solvent effects have a significant impact on the electrocatalytic reaction mechanisms. 28-33 Yet, these issues remain largely unexplored and poorly understood. Taking them into account and elucidating a comprehensive picture for Ni⁰-Ni^{δ+}-mediated C–C coupling is significantly meaningful for opening a new way for efficient C₃₊ production.

In this work, we theoretically investigated the role of Ni⁰-Ni^{∂+} on C−C coupling at the partial polarized nickel using the full-solvent ab initio molecular dynamics (AIMD) simulations with a slow-growth approach.^{34,35} Our findings indicate that the downward shift of the polarized Ni d-band center effectively weakens the adsorption strength of the two critical intermediates, namely *CO2 and *CO. As a direct outcome of this characteristic, *COOH forms more readily and remains stable in the polarized region. Furthermore, the mitigation of *CO poisoning allows for its further reduction within the polarized domain. After the hydrogenation of *CO to *CH $_x$ (x = 1, 2), *COOH and *CH_x can readily combine, with a much lower activation energy than the traditional *CO involved C-C coupling. Considering that oxidation serves as a common method for lowering the d-band center of metals, we propose that constructing M^0 - $M^{\delta+}$ (M= Fe, Rh, Pd, Co, Ru) domains could also be promising catalyst systems for facilitating C-C coupling by mediating their adsorption strength of key intermediates. Collectively, we elucidate the microscopic mechanisms by which metal polarization, as a simple yet powerful approach, can regulate intermediate thermodynamics to promote the formation of long-chain carbon products in electrochemical CO2 reduction.

RESULTS AND DISCUSSION

Catalyst Model Construction and Electronic Structure Analysis. Electrocatalysts derived from inorganic nickel oxygenates, exemplified by phosphate-derived nickel systems (denoted as PD-Ni), have demonstrated exceptional selectivity toward long-chain hydrocarbon production.²¹ Nevertheless, the fundamental mechanism governing the formation and evolution of active sites during catalytic operation remains a subject of ongoing debate.³⁶ To bridge this knowledge gap and establish a representative model system, we employ nickel phosphate (Ni₃(PO₄)₂) as a structural precursor to investigate the dynamic surface reconstruction processes under operational conditions. To accurately simulate the electrochemical environment, we systematically introduced $1-2(K^+ + e)$ ion pairs into the model system, thereby establishing a realistic representation of the electrode-electrolyte interface and solvent environment (Figure S1). Our analysis reveals that the introduction of $(K^+ + e)$ ion pairs significantly enhances the interfacial dynamical activity of phosphate (PO₄³⁻) groups,

as evidenced by their increased positional fluctuations and altered bond-length distributions (Figures S2, S3). Furthermore, the enhanced interfacial dynamics of phosphate ions facilitate the leaching behavior of surface phosphate groups. As illustrated in Figure S4, the specific adsorption of $(K^+ + e)$ ions on phosphate significantly lowers the reaction energy barrier and promotes its adsorption at the interface. This indicates that cations induce the activation of the precursor and the leaching of phosphate groups, further triggering reconstruction of the catalyst precursor and is generally observed in the cathodic corrosion of other metals. This phenomenon is supported by experimental results, where the P/Ni ratio in PD-Ni samples gradually decreased by approximately 1 atom % during the reaction. 21 Moreover, this suggests that phosphate groups may not participate in the formation of active sites under the final steady-state conditions. Another experimental observation is that Ni⁰ sites gradually increase from 0% to 13%, while the remaining species consist of $Ni^{\delta+21}$ This indicates that, as phosphate groups leach out, the catalytic activity is primarily governed by the cooperative effect of the Ni^0 - $Ni^{\delta+}$ domain. To further explore its impact on the eCO₂RR catalytic mechanism, we will employ corresponding models for analysis.

Based on the aforementioned analysis, we employed *O species to construct the $\mathrm{Ni^0\text{-}Ni^{\delta^+}}$ domain. As illustrated in Figure 1a, we systematically established a concentration gradient of *O coverage and ultimately identified 3/32 ML

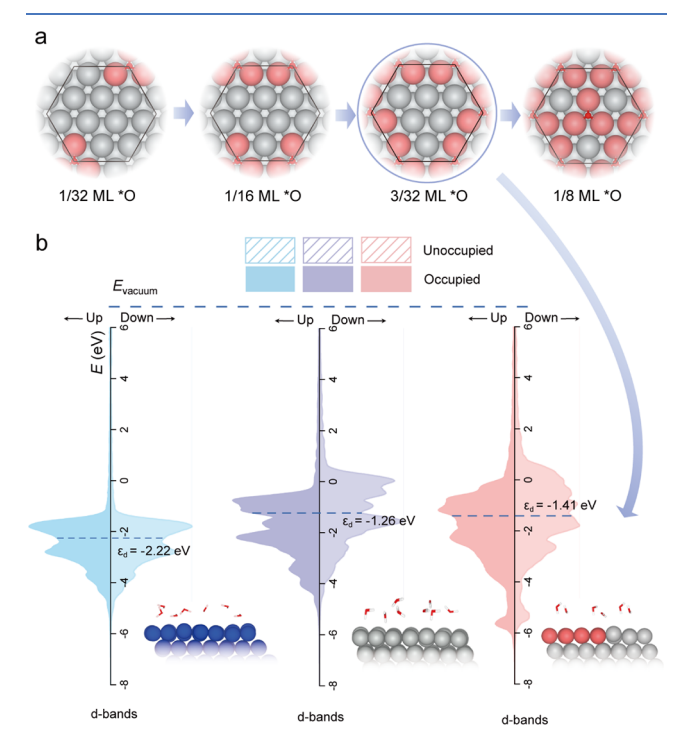


Figure 1. Electronic structure analysis of Cu (111), Ni (111), and Ni $_{pol}$ (111): (a) Ni $_{pol}$ (111) with four polarization degrees was constructed, and the surface oxygen atoms occupied 1/32, 1/16, 3/32, and 1/8 adsorption sites (ML *O), respectively (from left to right). Finally, Ni $_{pol}$ with 3/32 ML*O was selected as the model to be studied, for its proper adsorption sites of both polarized and nonpolarized. (b) The blue, purple, and red DOS plots represent Cu, Ni, and Ni $_{pol}$, respectively. The structures in the bottom-right corner illustrate their slab with solvated configurations. Solvated configurations can be found in Figure S11. In the slab model, blue spheres represent Cu atoms, gray spheres represent Ni atoms, and red spheres represent Ni $_{pol}$ atoms.

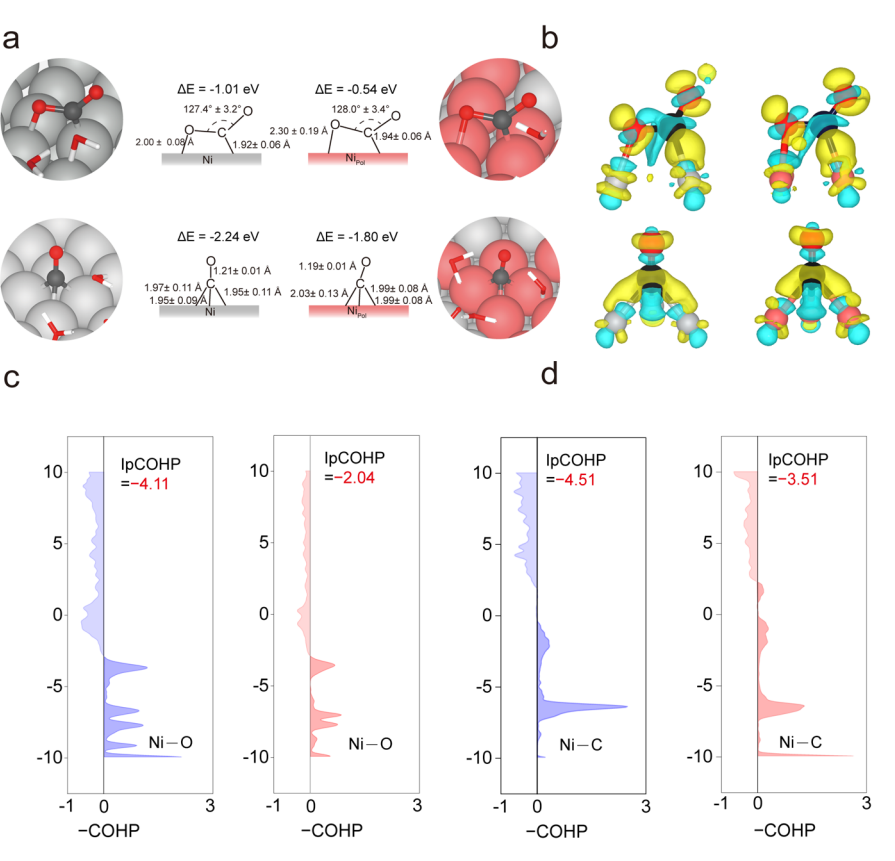


Figure 2. Comprehensive analysis of the *CO_2 -to- *CO conversion reaction mechanism: (a) *CO_2 and *CO adsorption configurations and corresponding adsorption energies on Ni and Ni_{pol}; (b) Differential charge density isosurfaces for *CO_2 and *CO adsorption: yellow represents electron accumulation and cyan denotes electron depletion (Isovalue = 0.0067 e Å⁻³); (c) COHP analysis for Ni–O bonds between nickel atom from surface and oxygen atom from *CO_2 ; (d) COHP analysis for Ni–C bonds between nickel atom from surface and carbon atom from *CO ; in (c) and (d) purple represents metallic Ni, red represents Ni_{pol}.

*O as the optimal model system. This selection was primarily based on the observation that both insufficient and excessive *O coverage (e.g., 1/32 ML and 1/8 ML *O, respectively) would result in inadequate Ni^{δ+}/Ni⁰ regions, thereby hindering the investigation of their influence on key reaction intermediates. The partially polarized Ni (111) (denoted as Nipol) was developed by introducing oxygen adsorb on surfaces. Considering the solvent environment (e.g., water) under real experimental conditions, *O may convert into *OH. Therefore, it is essential to systematically evaluate their impact on model construction. Then we calculate their adsorption energies on Ni(111) (Figure S5) and analyzing the free energy pathway for the *O-to-*OH-to-*H₂O transition (Figure S6). The calculated Gibbs free energy changes for the *O→*OH and *OH \rightarrow *H₂O transitions are -0.05 eV and -0.08 eV, respectively. The minimal energy differences indicate thermodynamically reversible interconversions and dynamic coexistence of *O, *OH. Subsequently, we investigate how these two species locally oxidize nickel atoms to a valence state of +0.22 e (*O) and +0.18 e (*OH), as confirmed by Bader charge analysis (Figures S7, S8). This slight charge difference suggests comparable electronic perturbation magnitudes between the two models with different adsorbed species. Therefore, we use models with *O in Figure 1a to analyze the influence of the Ni^0 - $Ni^{\delta+}$ domain on the eCO₂RR mechanism.

Based on above discussion, we then examined the d-band structures of Ni (111) and partially polarized Ni $_{\rm pol}$ (111) to gain a fundamental understanding of these materials from the perspective of electronic structure. The result of Cu (111) was

also presented as a comparison (Figure 1b, S9). By referencing the energy levels of the three systems, a direct comparison of their density of state (DOS) profiles reveals that the d-band center (ε_d) of Cu (-2.22 eV) is notably lower than that of Ni (-1.26 eV) relative to the Fermi level (Figure S10). Consequently, when adsorbates interact with Ni, the resulting antibonding orbitals originating from orbital splitting are more likely to occupy states above the Fermi level, leading to their stronger adsorption on Ni compared to Cu. Nevertheless, stronger adsorption does not always equate to better performance in catalysis, as dictated by the Sabatier principle.⁴⁰ In fact, Cu has emerged as a popular metal for CO₂ reduction precisely because its d-band center is well-positioned, resulting in moderate *CO adsorption energy. 41 In contrast, Ni is considered suffering from *CO poisoning due to its excessively strong *CO adsorption. 42-44 Upon introducing oxygen into Ni, chemical bonds form between the Ni and oxygen atoms. Due to the high electronegativity of oxygen, electrons are drawn from Ni toward the oxygen atoms, which reduces the delectron density of Ni, thus resulting a lower d-band center of polarized Ni (-1.41 eV). It can be anticipated that a weakened adsorption for intermediates during the CO₂ reduction will be achieved on Nipol, thereby alleviating the poisoning effect on

Effect of Polarization on the Reaction Mechanism. The adsorption energies of the two key intermediates, *CO₂ and *CO, on Ni and Ni_{pol} were calculated by averaging over ten selected configurations from the AIMD trajectories (details in Figures S12, S13). On both surfaces, *CO₂ exhibited a

ACS Catalysis pubs.acs.org/acscatalysis Research Article

bidentate adsorption mode on both surfaces, with one carbon and one oxygen atom binding to atop sites of the surface atoms. In contrast, *CO tended to adsorb at hollow sites. The adsorption energies of *CO2 and *CO on Ni were found to be -1.01 eV and -2.24 eV, respectively. Notably, we also calculated the adsorption energies of *CO₂ and *CO on Ni in the absence of water environment, which were 0.96 and 0.15 eV higher than those in the presence of water (Figures S12 and S13). This highlights the importance of considering the solvation environment, especially for *CO2, which forms strong hydrogen bonds with the interfacial water (Figure S13). 45,46 When *CO_2 and *CO adsorb on Ni_{pol} their adsorption energies become notably less negative (-0.54 eV for *CO2 and -1.80 eV for *CO) in the solvation environment, accompanied by distinct changes in their adsorption configurations. Specifically, the Ni-O bonds between *CO₂ and the interface lengthen, leading to reduced charge transfer between Ni and O (Figure 2b) and a significant decrease in the bond strength, as evidenced by the less negative IpCOHP (integrated crystal orbital Hamilton population) values (Figure 2c). For *CO, the Ni-C bond also undergoes elongation (Figure 2a), leading to weakened bond strength (Figure 2b). The decreased charge accumulation on the carbon atom indicates reduced back-donation from the metal to the antibonding orbitals of *CO (Figure 2d), thereby shortening the C-O bond (Figure 2a). Collectively, the altered d-band electronic structure in the polarized region significantly impacts the adsorption behavior of *CO₂ and *CO.

Subsequently, we employed the slow-growth method to evaluate the kinetic barriers of the transformation of *CO₂ into *CO (Figure 3). On the Ni_{pol} surface, the adsorption energy of

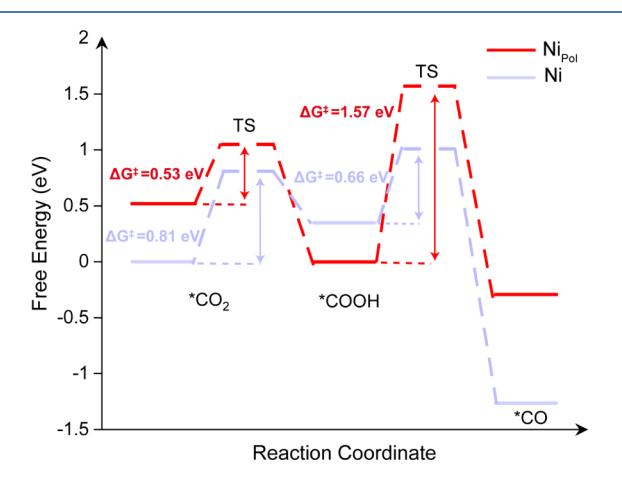


Figure 3. Free energy pathway diagram for *CO₂-to-*COOH-to-*CO conversion on Ni and Ni_{pol}. TS: transitional state.

*CO₂ becomes less exergonic (while still remaining favorable), which substantially lowers the activation barrier (0.53 eV) for the conversion of *CO₂ to the *COOH intermediate. Conversely, on pristine Ni, the excessively strong adsorption of *CO₂ induces a degree of catalytic poisoning, resulting in a comparatively elevated activation energy of 0.81 eV. In the *COOH-to-*CO conversion process, however, the scenario is markedly different. The diminished adsorption strength of *CO on Ni_{pol} reduces the exothermicity of the *COOH-to-*CO transformation, thereby elevating the activation barrier to 1.57 eV. Conversely, on pristine Ni, the strongly exergonic *CO adsorption confers an inherent thermodynamic advant-

age for *COOH hydrogenation, yielding a substantially lower barrier of 0.66 eV, further details are provided in Figures S15 and S16. This finding is consistent with the Brønsted–Evans–Polanyi (BEP) principle, ⁴⁷ which posits a positive correlation between thermodynamic driving force and activation energy. As a result, the activated *COOH species tend to remain anchored at the interface on Ni_{pol}, whereas on pure Ni, *COOH is more inclined to undergo further reduction to *CO.

The occurrence of C–C coupling requires the coadsorption of two carbon-containing species in a localized region. Experimental studies have shown that feeding CO₂ together with CO or HCHO yields significantly higher amounts of multicarbon products compared to using CO₂ or CO alone.²¹ This indicates that the species involved in C-C coupling are likely positioned such that one precedes *CO formation and the other follows it. In the region of polarized Ni, *COOH can remain adsorbed for extended periods due to the high energy barrier for its conversion to *CO. We subsequently analyzed the energy required for further hydrogenation of *CO to explore the formation of another potential intermediate. In the CO₂RR process, *CO can undergo two potential hydrogenation pathways: one involves hydrogenation at the oxygen end to form *COH, 48 and the other at the carbon end to form *CHO.^{7,49,50} Both pathways can proceed via the Eley-Rideal (ER) or Langmuir-Hinshelwood (LH) mechanism. After a comprehensive evaluation of these possibilities, we found that only the hydrogenation of *CO to *CHO via the LH mechanism is energetically favorable in the Ni_{pol} region (0.82 eV, Figure 4). All other pathways, whether on Nipol or pristine Ni, exhibit high energy barriers or lack inflection points in the energy profile, indicating that these processes are unlikely to occur (Figure 4a, S17 and S18). It is evident, as illustrated in Figure 3, that the formation of *CO within the polarized Ni region is inherently challenging. Nonetheless, we discovered that *CO generated on the pristine Ni region can readily migrate to the polarized domain with a relatively low energy barrier (0.35 eV), revealing a synergistic interplay between the polarized and nonpolarized regions (Figure S19). Essentially, the pristine Ni region acts as a source for producing *CO necessary for subsequent transformations, while the polarized region, due to its attenuated adsorption strength and potentially lower activation barriers in accordance with the BEP relationship, facilitates the further hydrogenation of *CO.

The hydrogenation step of *CO is widely regarded as the rate-determining step in the reduction of CO2 to C1 products.^{7,51} Once this barrier is overcome, the subsequent steps generally become energetically favorable, making them potential candidates for C-C coupling.⁵² To capture the overall energetic trends of C-C coupling, we evaluated the feasibility of coupling *CO, *CHO, *CHOH, *C, *CH, *CH₂ and *CH₃ with *CO₂, *COOH and *CO (Figure 5a and b), representing typical C-C coupling patterns.⁵³ All optimized structures, including the initial states and final states are presented in Figures S20 and S21. Notably, Due to the computational cost of AIMD simulations, we performed thermodynamic energy calculations based solely on structural optimization without considering solvent effects. It can be observed that among *CO₂, *COOH, and *CO, the former two serve as more favorable building blocks for C-C coupling, exhibiting consistently lower reaction energies for the coupling process. In the case of species derived from the further reduction of *CO, the thermodynamic feasibility of C-C

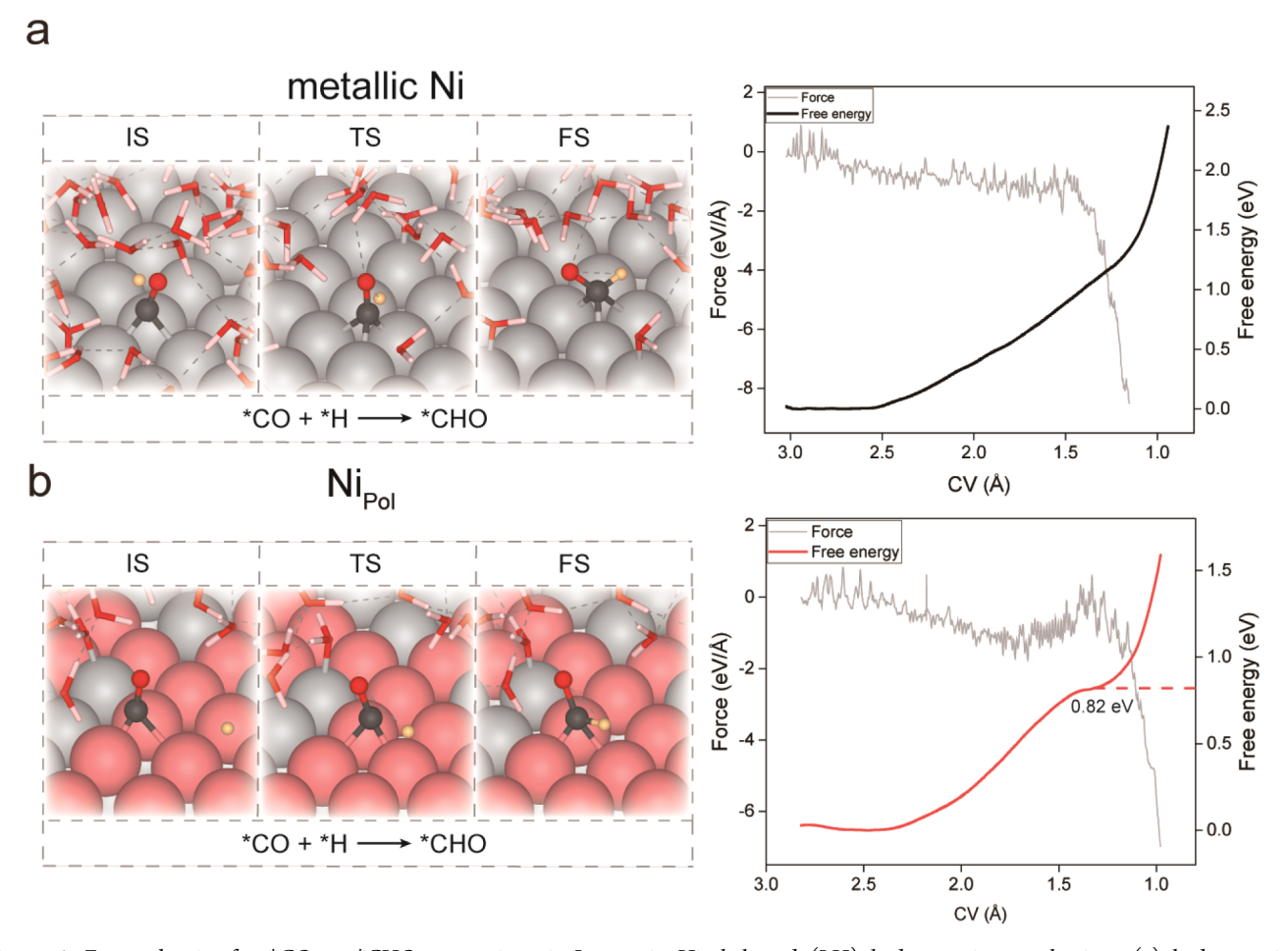


Figure 4. Energy barrier for *CO to *CHO conversion via Langmuir—Hinshelwood (LH) hydrogenation mechanism: (a) hydrogenation structures and energy profile on Ni (111); (b) hydrogenation structures and energy profile on Ni_{pol} (111).

coupling tends to improve with increasing reduction levels. This observation suggests that *CO, contrary to conventional assumptions, may not an optimal species for C-C coupling—a conclusion that can be rationalized from a chemical perspective.^{54,55} *CO possesses a highly stable electronic configuration and forms a robust bond with the Ni and Nipol surface, evidenced by its strongly negative adsorption energy (Figure 2a). In contrast, *CO₂, due to its unoccupied antibonding orbitals and highly electronegative oxygen atoms, can undergo partial reduction at the interface to yield a more reactive species (*CO₂⁻), thereby significantly enhancing its catalytic reactivity. ⁵⁶ Similarly, the antibonding orbitals of the carbonyl group in *COOH, coupled with the electronegativity of the hydroxyl group, facilitate efficient electron acceptance during adsorption, promoting bond rearrangements and the formation of new C-C bonds. Interestingly, in the field of electrochemical C-N coupling toward urea using CO₂ and nitrogen oxides as reactants, *CO₂ or *COOH, rather than *CO, has also been widely reported as the coupling species. 33,57-59 Regarding the intermediates formed after the hydrogenation of *CO, the weakening of the triple bond, followed by the complete dissociation of the oxygen, imparts a degree of radical character to the carbon species. This shift in electronic structure effectively reduces the energy barrier of C-C coupling, thereby facilitating the C-C coupling.

Ni⁰-Ni⁰⁺ Facilitates Asymmetric C–C Coupling. To validate the robustness of this conclusion, we employed the

slow-growth method with full solvent environment to calculate the kinetic barriers for several C-C coupling pathways, including *CO-*CO, *CO2-CH2, *COOH-*CH, and *COOH-*CH2. All figures and energy files can be found in Figures S22, S23. The results indicate that the dimerization of *CO is highly challenging both on Ni and Nipol surfaces, with activation energies exceeding 1.7 eV. In contrast, the coupling pathways involving *COOH and *CO2 exhibit significantly lower kinetic barriers, with the *CO2-*CH2 and *COOH-*CH₂ couplings showing activation barriers of 0.27 and 0.36 eV, respectively, suggesting a higher likelihood of occurrence under practical conditions. Interestingly, this conclusion holds true for Cu as well. Our calculations revealed that the kinetic barriers of coupling pathways involving *COOH and *CO2 on Cu are consistently lower than those of *CO-*CO coupling. The work by Cheng et al. provides a more comprehensive analysis of the energy comparisons for C-C coupling involving *CO2 and *CO with other carbon species on Cu, demonstrating that *CO2 is a more favorable coupling species than *CO.60 This suggests that our analysis may possess a certain degree of general applicability. Another noteworthy point is that the energy barriers for C–C coupling on polarized Ni are consistently lower than those on pristine Ni. This decrease in barriers is likely attributed to the weakening of adsorption strength for carbon-containing species due to polarization, which in turn alleviates the poisoning effect. Additionally, we calculated the energy barriers for the conversion of *CH₂ to *CH₃. If *CH₃ forms and subsequently

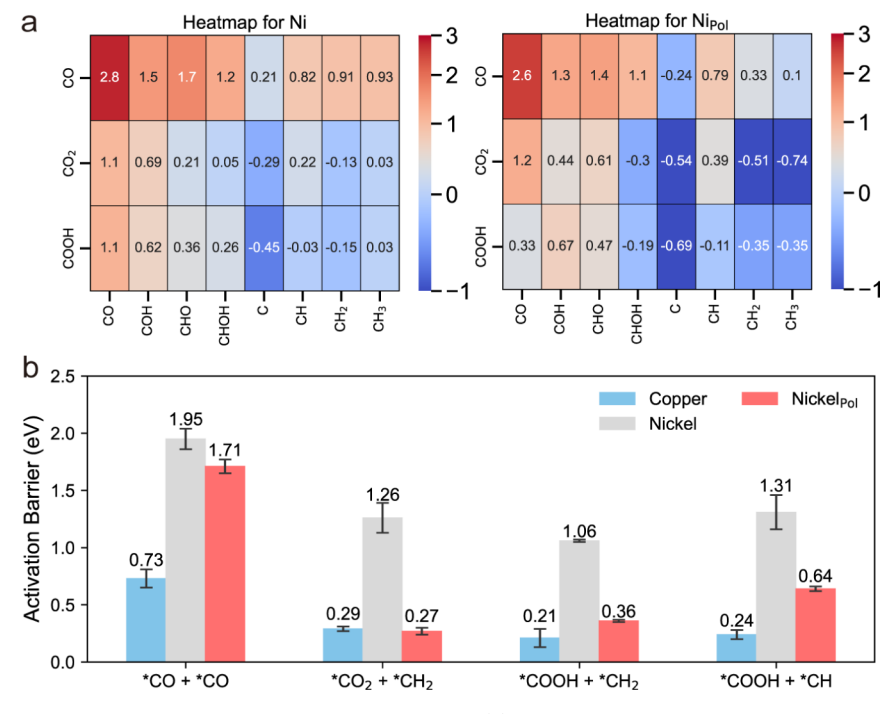


Figure 5. Thermodynamic and kinetic analysis of C–C coupling pathways: (a) Heatmap analysis of thermodynamic reaction energies for various C–C coupling patterns on Ni and Ni_{pol}. The thermodynamically favorable patterns ($\Delta E_{free} < 0$) are highlighted in blue, while the unfavorable patterns ($\Delta E_{free} > 0$) are highlighted in reddish-brown. (b) Kinetic energy barrier analysis of *CO+*CO, *CO₂+*CH₂, *COOH+*CH₂, *COOH+*CH on Cu, Ni, and Ni_{pol}. Ni_{pol} means C–C coupling process occurs on Ni⁰-Ni^{\delta+} domain.

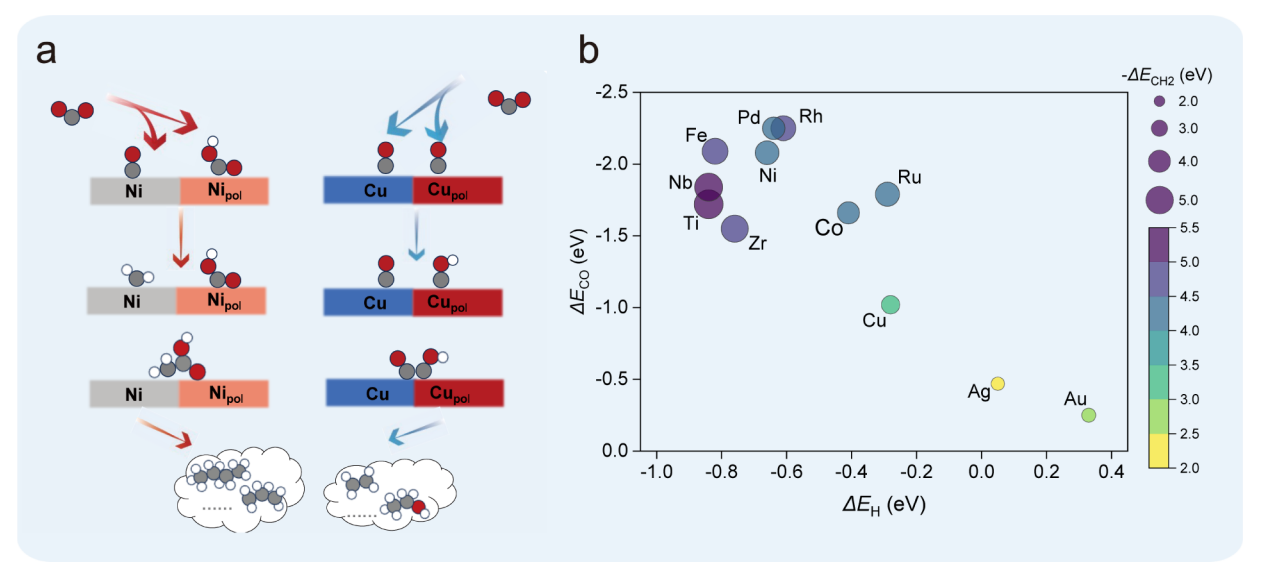


Figure 6. Scheme of (a) different mechanisms of C–C coupling for Ni 0 -Ni $^{\delta+}$ and Cu 0 -Cu $^{\delta+}$ regions; (b) Colormap plot for analyzing the potential of transition metal catalysts (Ti, Nb, Zr, Fe, Rh, Ni, Pd, Co, Ru, Cu, Ag, Au) for long-chain hydrocarbons synthesis, with the *x*-axis for *CO adsorption energy, *y*-axis for *H adsorption energy, and bubble size as well as its color for negative *CH₂ adsorption energy. More details are provided in Figures S25–27.

engages in C–C coupling, the growth of the carbon chain will terminate. Thus, to achieve the formation of long-chain hydrocarbons, it is crucial to inhibit the generation of *CH_3 . We found that the energy barriers for this step are 0.66 eV on pristine Ni and 0.94 eV on Ni $_{pol}$, respectively (Figure S24). This energy barrier is sufficiently high to effectively prevent *CH_3 formation and thus serves as another key factor in enabling the experimental formation of even C_6 products.

A schematic diagram illustrating how ${\rm Ni^0}$ - ${\rm Ni^{\delta^+}}$ facilitates C—C coupling is presented in Figure 6a. For comparison, the

general mechanism of Cu^0 - $Cu^{\delta+}$ promoting C–C coupling is also depicted. In the Ni system, the primary role of the polarized region is to weaken the adsorption of carbon-containing species, allowing *COOH to remain as a stable intermediate during the conversion of *CO₂ to *CO. Concurrently, *CO generated in the nonpolarized region can migrate to the polarized region, where it undergoes further reduction to *CH_x species, ultimately enabling an insertion-type C–C coupling process involving *CH_x. In the Cu system, due to the conversion of CO₂ to CO is a rapid process, the

primary role of the polarized region is to create a distinct *CO adsorption state with an electronic structure different from that of *CO in the nonpolarized region. This differentiation can enhance *CO-CO coupling or facilitate the reduction of *CO to *COH/*CHO, enabling subsequent *CO-*COH or *CO-*CHO coupling. 10,11,13,18 The key distinction between the Ni and Cu systems lies in Ni's avoidance of reaction pathways that utilize *CO as the C-C coupling species, instead favoring *CO₂ and/or *COOH based C-C coupling. This unique mechanism stems from the inherently strong adsorption of carbon-containing species on Ni. Polarization, such as through oxygen doping, raises the metal's oxidation state and shifts the d-band center away from the Fermi level. This effectively mitigates the poisoning effect of intermediates, preventing them from becoming trapped in thermodynamically stable states, such as *CO adsorption.

Extension of Mechanism to Other Transition Metals and Open Questions. Since elevating the oxidation state of metals through polarization to lower the d-band center represents a broadly applicable strategy, we were inspired to hypothesize that other metals with carbon-species affinities akin to Ni could also facilitate long-chain hydrocarbons via polarization. To identify potential candidates for long-chain hydrocarbons formation using this approach, we performed high-throughput calculations of the adsorption energies of key intermediates (*CO, *CH₂, *H) across various metals (M = Ti, Nb, Zr, Fe, Rh, Ni, Pd, Co, Ru, Cu, Ag, Au). The calculation of *CO adsorption energy can be utilized to evaluate the affinity of different metal interfaces toward carbon oxides (*CO₂, *COOH and *CO), while strong *CH₂ adsorption maximizes the possibility for the chain growth toward long-chain carbon products. We also calculated adsorption energies of *H to evaluate the potential for HER side reactions. To enhance screening efficiency, we performed only structural optimizations without employing molecular dynamics methods. The solvent environments were also not included since the adsorption energies of *CO, *CH2, and *H are generally considered to be relatively unaffected by solvation effects. The results (Figure 6b) reveal that Ru, Rh, Fe, Co and Pd possess adsorption energies for key intermediates comparable to those of Ni, indicating their possibility for facilitating the formation of long-chain carbon product through polarization strategies. In contrast, Ti, Nb, and Zr exhibit excessively strong adsorption of carbon-containing species. Cu, with its moderate *CO adsorption strength, favors *CO-CO coupling, whereas Au and Ag, due to their weak *CO affinity, predominantly produce CO as the primary product. Notably, Co has recently been confirmed as capable of achieving longchain carbon products in CO2RR through the strategic construction of polarized-nonpolarized regions.⁶¹ Although similar evidence is so far lacking for Fe, Pd, Ru, and Rh, the demonstrated ability of Fe phosphides and Pd alloys to produce multicarbon products underscores their promising potential.62-65 Future work will involve constructing models with tunable polarization on various metals and applying machine learning to uncover universal relationships between polarization, d-band shifts, and the adsorption energies of key CO₂ reduction intermediates, aiming to build a more comprehensive mechanistic framework for long-chain product formation.

Based on the above findings, we propose that the Ni⁰-Ni³⁺ domain, by modulating the formation of various reaction intermediates, enables an asymmetric C–C coupling mecha-

nism that may also hold similar potential on other transition metals such as Fe, Pd, Ru, and Rh. It should be acknowledged that although we conducted an in-depth investigation into the thermodynamic and kinetic processes of the eCO₂RR on a nickel-based catalyst—leveraging AIMD and the slow-growth method in a solvent environment to systematically investigate the impact of metal polarization on the thermodynamic states of intermediates (an effect primarily governed by the intrinsic properties of the metal)—other factors influencing the reaction mechanism were not considered. For instance, factors such as potential and pH, which are relevant to the electrochemical environment, were not considered in this work. Despite the fact that polarization enables the feasibility of long-chain carbon products, the selectivity remains relatively low, with hydrogen gas often being the dominant product. 21,61 This indicates that additional strategies need to be implemented to suppress the competing HER side reaction. Building on the polarization strategy, incorporating metals with low hydrogen affinity, such as Ga and Al, could be an effective approach. On Cu, the addition of Ga and Al has been demonstrated to successfully suppress HER and promote the formation of multicarbon products. 66,67 On Ni, even the sole incorporation of Ga, without the construction of polarized regions, has been shown to yield multicarbon products. 24,25 Additionally, electrolyte engineering to change interfacial environment presents another promising avenue for C-C coupling promotion.⁶⁸ This can be achieved by reducing water activity, introducing surface-modified molecules, or altering surface morphology.

CONCLUSIONS

In this study, we explored the influence of Ni^0 - $Ni^{\delta+}$ on C-C coupling in partially polarized nickel through full-solvent ab initio molecular dynamics (AIMD) simulations combined with the slow-growth methodology. The results reveal that the dband center shift in polarized Ni significantly diminish the poisonous effect of two key intermediates, namely *CO2 and *CO, thereby enhancing their reactivity. As a direct result of this characteristic, *COOH is more easily formed and stays in the polarized region. Additionally, the *CO generated in the nonpolarized region can migrate to the polarized region, where it undergoes further hydrogenation to form *CH_x species. The *COOH and *CH_x species can efficiently combine, resembling the chain elongation process of Fischer-Tropsch synthesis, with a significantly lower activation energy compared to traditional *CO-mediated C-C coupling pathways. Given that oxidation is a general approach to lowering the d-band center of metals, we suggest that creating M^0 - $M^{\delta+}$ domains may serve as an efficient strategy to enhance C-C coupling on Fe, Ru, Rh, Co, and Pd metals that exhibit similar adsorption characteristics of key species like Ni. In summary, we unveil the microscopic mechanisms through which metal polarization, as a straightforward yet potent strategy, modulates intermediate thermodynamics to drive the formation of long-chain carbon products in electrochemical CO₂ reduction.

METHODS

First, in model construction stage, the (001) facet of $\mathrm{Ni_3(PO_4)_2}$ was employed, and 30 explicit water molecules were incorporated to establish the initial configuration for ab initio molecular dynamics (AIMD) simulations. Subsequently, a 20 ps molecular dynamics simulation was performed to

achieve system equilibration and the structural configurations, along with the temporal evolution of temperature and total energy fluctuations during the simulations, are comprehensively presented in Figure S1.

Then the Ni(111) surface, as a primary Miller index facet of polycrystalline nickel⁷⁰ and is notably selective in catalyzing long-chain hydrocarbon synthesis, particularly when alloyed or doped with other elements. 22,71,72 In this article, we utilize the Ni(111) surface and partially polarized Ni(111) surface models to simulate metallic nickel and nickel-based catalysts polarized by highly electronegative species, such as oxygen. Additionally, we include a Cu(111) slab as a control to compare typical *CO-dominant reaction mechanisms.⁷³ All slabs were constructed using a four-layer 4 × 4 supercell with a vacuum region of approximately 15 Å along the z-axis to prevent interactions between periodic images. To simulate a fully solvated model, 30 water molecules were explicitly added above the Cu and (partially polarized) Ni surfaces, creating water layers with thickness of approximate 10 Å. Full-scale models of the three systems discussed are shown in Figures S9 and S11.

Density functional theory (DFT) calculations were carried out using the Vienna Ab initio Simulation Package (VASP)^{74,75} with the projector-augmented-wave (PAW) method.⁷⁶ To account for electron exchange-correlation interactions, we applied the Perdew-Burke-Ernzerhof (PBE) functional within the framework of the generalized gradient approximation (GGA).⁷⁷ Additionally, Grimme's D3 dispersion correction was included to account for van der Waals interactions.⁷⁸ The full solvated environment is simulated by AIMD simulations to model the dynamics of water molecules and the hydrogen bond network. The slow-growth method,34,35 applied with VASP, is employed to obtain the energy profile under explicit water conditions. The adsorption energies in solvent environment is obtained after performing self-consistent calculations on structures parallel-extracted from a 10 ps trajectory, where the adsorbate has been fully stabilized.

We conducted density of states (DOS) calculations and Bader charge analysis using the Device Studio integrated Projector Augmented-Wave method package (DS-PAW). To further examine the bonding interactions between the adsorbate and the interface, we applied crystal orbital Hamiltonian population (COHP) calculations, providing a detailed evaluation of bond lengths within the interface structure. 99,80 More details of our calculations can be found in the Supporting Information.

ASSOCIATED CONTENT

Data Availability Statement

Crucial model structure configurations and DFT-based calculation details are available at https://github.com/dinghw49/ACS-Catalysis-Pol-Ni.git

Supporting Information

The Supporting Information is available free of charge at https://pubs.acs.org/doi/10.1021/acscatal.4c07353.

Details of the computational models and equations used for AIMD simulations, all adsorbate configurations, free energy files for the eCO_2RR mechanism, the C-C coupling process on nickel-based catalysts, and adsorption energies for other transition metals are provided (PDF)

AUTHOR INFORMATION

Corresponding Authors

Shunning Li — School of Advanced Materials, Peking University, Shenzhen Graduate School, Shenzhen 518000, China; orcid.org/0000-0002-5381-6025; Email: lisn@pku.edu.cn

Feng Pan — School of Advanced Materials, Peking University, Shenzhen Graduate School, Shenzhen 518000, China; orcid.org/0000-0002-8216-1339; Email: panfeng@pkusz.edu.cn

Shisheng Zheng — College of Energy, Xiamen University, Xiamen 361000, China; orcid.org/0009-0000-4529-7440; Email: zhengss@xmu.edu.cn

Authors

Haowen Ding — School of Advanced Materials, Peking University, Shenzhen Graduate School, Shenzhen 518000, China

Wenwei Cai – School of Advanced Materials, Peking University, Shenzhen Graduate School, Shenzhen 518000, China

Xinzhe Yang — School of Advanced Materials, Peking University, Shenzhen Graduate School, Shenzhen 518000, China; ⊚ orcid.org/0009-0008-1921-0629

Yu Zhang — School of Advanced Materials, Peking University, Shenzhen Graduate School, Shenzhen 518000, China

Complete contact information is available at: https://pubs.acs.org/10.1021/acscatal.4c07353

Author Contributions

§H.D. and W.C. contributed equally to this work. The College of Energy, Xiamen University, is the primary contributing institution.

Notes

The authors declare no competing financial interest.

ACKNOWLEDGMENTS

The authors acknowledge financial support from the Guangdong Basic and Applied Basic Research Foundation (2020A1515110843), Chemistry and Chemical Engineering Guangdong Laboratory (Grant No. 1922018), Fundamental Research Funds for the Central Universities (20720240054), National Natural Science Foundation of China (22402163, 22109003), Natural Science Foundation of Shenzhen (JCYJ20190813110605381), and the Major Science and Technology Infrastructure Project of the Material Genome Big-Science Facilities Platform supported by the Municipal Development and Reform Commission of Shenzhen.

REFERENCES

- (1) Yan, T.; Chen, X.; Kumari, L.; Lin, J.; Li, M.; Fan, Q.; Chi, H.; Meyer, T. J.; Zhang, S.; Ma, X. Multiscale CO₂ Electrocatalysis to C₂₊ Products: Reaction Mechanisms, Catalyst Design, and Device Fabrication. *Chem. Rev.* **2023**, *123* (17), 10530–10583.
- (2) Nitopi, S.; Bertheussen, E.; Scott, S. B.; Liu, X.; Engstfeld, A. K.; Horch, S.; Seger, B.; Stephens, I. E. L.; Chan, K.; Hahn, C.; et al. Progress and Perspectives of Electrochemical CO₂ Reduction on Copper in Aqueous Electrolyte. *Chem. Rev.* **2019**, *119* (12), 7610–7672.
- (3) Aresta, M.; Dibenedetto, A.; Angelini, A. Catalysis for the valorization of exhaust carbon: from CO₂ to chemicals, materials, and fuels. technological use of CO₂. *Chem. Rev.* **2014**, *114* (3), 1709–1742.

- (4) Wang, X.; Wang, Z.; García de Arquer, F. P.; Dinh, C.-T.; Ozden, A.; Li, Y. C.; Nam, D.-H.; Li, J.; Liu, Y.-S.; Wicks, J.; et al. Efficient electrically powered CO₂-to-ethanol via suppression of deoxygenation. *Nat. Energy* **2020**, *5* (6), 478–486.
- (5) Chen, X.; Chen, J.; Alghoraibi, N. M.; Henckel, D. A.; Zhang, R.; Nwabara, U. O.; Madsen, K. E.; Kenis, P. J. A.; Zimmerman, S. C.; Gewirth, A. A. Electrochemical CO₂-to-ethylene conversion on polyamine-incorporated Cu electrodes. *Nat. Catal.* **2021**, *4* (1), 20–27.
- (6) Li, F.; Thevenon, A.; Rosas-Hernandez, A.; Wang, Z.; Li, Y.; Gabardo, C. M.; Ozden, A.; Dinh, C. T.; Li, J.; Wang, Y.; et al. Molecular tuning of CO₂-to-ethylene conversion. *Nature* **2020**, *577* (7791), 509–513.
- (7) Cheng, T.; Xiao, H.; Goddard, W. A. Full atomistic reaction mechanism with kinetics for CO reduction on Cu(100) from ab initio molecular dynamics free-energy calculations at 298 K. *Proc. Natl. Acad. Sci. U. S. A.* 2017, 114 (8), 1795–1800.
- (8) Zhuang, T.-T.; Liang, Z.-Q.; Seifitokaldani, A.; Li, Y.; De Luna, P.; Burdyny, T.; Che, F.; Meng, F.; Min, Y.; Quintero-Bermudez, R.; et al. Steering post-C—C coupling selectivity enables high efficiency electroreduction of carbon dioxide to multi-carbon alcohols. *Nat. Catal.* **2018**, *1* (6), 421–428.
- (9) Liu, H.; Yang, C.; Bian, T.; Yu, H.; Zhou, Y.; Zhang, Y. Bottom-up Growth of Convex Sphere with Adjustable Cu(0)/Cu(1) Interfaces for Effective C_2 Production from CO_2 Electroreduction. *Angew. Chem., Int. Ed.* **2024**, 63 (28), No. e202404123.
- (10) Yuan, X.; Chen, S.; Cheng, D.; Li, L.; Zhu, W.; Zhong, D.; Zhao, Z. J.; Li, J.; Wang, T.; Gong, J. Controllable Cu°-Cu⁺ Sites for Electrocatalytic Reduction of Carbon Dioxide. *Angew. Chem., Int. Ed.* **2021**, *60* (28), 15344–15347.
- (11) Zhang, T.; Xu, S.; Chen, D.-L.; Luo, T.; Zhou, J.; Kong, L.; Feng, J.; Lu, J.-Q.; Weng, X.; Wang, A.-J.; Li, Z.; et al. Selective Increase in CO_2 Electroreduction to Ethanol Activity at Nanograin-Boundary-Rich Mixed Cu(I)/Cu(0) Sites via Enriching co-Adsorbed CO and Hydroxyl Species. *Angew. Chem., Int. Ed.* **2024**, 63 (33), No. e202407748.
- (12) Zhou, Y.; Yao, Y.; Zhao, R.; Wang, X.; Fu, Z.; Wang, D.; Wang, H.; Zhao, L.; Ni, W.; Yang, Z.; Yan, Y.-M.; et al. Stabilization of Cu⁺ via Strong Electronic Interaction for Selective and Stable CO₂ Electroreduction. *Angew. Chem., Int. Ed.* **2022**, *61* (31), No. e202205832.
- (13) Cai, R.; Sun, M.; Yang, F.; Ju, M.; Chen, Y.; Gu, M. D.; Huang, B.; Yang, S. Engineering Cu(I)/Cu(0) interfaces for efficient ethanol production from CO_2 electroreduction. *Chem* **2024**, *10* (1), 211–233.
- (14) Cao, X.; Ren, S.; Zhang, X.; Fan, Q.; Chen, Q.; Yang, J.; Mao, J. Identification of $\text{Cu}^{\circ}/\text{Cu}^{+}/\text{Cu}^{\circ}$ interface as superior active sites for CO_2 electroreduction to C_{2+} in neutral condition. *Chem* **2024**, *10* (7), 2089–2102.
- (15) Meng, H.; Yang, Y.; Shen, T.; Yin, Z.; Wang, L.; Liu, W.; Yin, P.; Ren, Z.; Zheng, L.; Zhang, J.; Xiao, F.-S.; et al. Designing Cu0-Cu + dual sites for improved C-H bond fracture towards methanol steam reforming. *Nat. Commun.* **2023**, *14* (1), 7980.
- (16) Arán-Ais, R. M.; Scholten, F.; Kunze, S.; Rizo, R.; Roldan Cuenya, B. The role of in situ generated morphological motifs and $Cu(_1)$ species in C_{2+} product selectivity during CO_2 pulsed electroreduction. *Nat. Energy* **2020**, 5 (4), 317–325.
- (17) Favaro, M.; Xiao, H.; Cheng, T.; Goddard, W. A., 3rd; Yano, J.; Crumlin, E. J. Subsurface oxide plays a critical role in CO₂ activation by Cu(111) surfaces to form chemisorbed CO₂, the first step in reduction of CO₂. *Proc. Natl. Acad. Sci. U. S. A.* **2017**, *114* (26), 6706–6711.
- (18) Xiao, H.; Goddard, W. A.; Cheng, T.; Liu, Y. Cu metal embedded in oxidized matrix catalyst to promote CO₂ activation and CO dimerization for electrochemical reduction of CO₂. *Proc. Natl. Acad. Sci. U. S. A.* **2017**, 114 (26), 6685–6688.
- (19) Zhou, Y.; Che, F.; Liu, M.; Zou, C.; Liang, Z.; De Luna, P.; Yuan, H.; Li, J.; Wang, Z.; Xie, H.; et al. Dopant-induced electron localization drives CO₂ reduction to C₂ hydrocarbons. *Nat. Chem.* **2018**, *10* (9), 974–980.

- (20) Liu, X.; Schlexer, P.; Xiao, J.; Ji, Y.; Wang, L.; Sandberg, R. B.; Tang, M.; Brown, K. S.; Peng, H.; Ringe, S.; Hahn, C.; et al. pH effects on the electrochemical reduction of $CO_{(2)}$ towards C_2 products on stepped copper. *Nat. Commun.* **2019**, *10* (1), 32.
- (21) Zhou, Y.; Martín, A. J.; Dattila, F.; Xi, S.; López, N.; Pérez-Ramírez, J.; Yeo, B. S. Long-chain hydrocarbons by CO₂ electro-reduction using polarized nickel catalysts. *Nat. Catal.* **2022**, *5* (6), 545–554.
- (22) Calvinho, K. U. D.; Laursen, A. B.; Yap, K. M. K.; Goetjen, T. A.; Hwang, S.; Murali, N.; Mejia-Sosa, B.; Lubarski, A.; Teeluck, K. M.; Hall, E. S.; et al. Selective CO₂ reduction to C₃ and C₄ oxyhydrocarbons on nickel phosphides at overpotentials as low as 10 mV. *Energy Environ. Sci.* **2018**, *11* (9), 2550–2559.
- (23) Vos, R. E.; Koper, M. T. M. Nickel as Electrocatalyst for CO((2)) Reduction: Effect of Temperature, Potential, Partial Pressure, and Electrolyte Composition. *ACS Catal.* **2024**, *14* (7), 4432–4440.
- (24) Paris, A. R.; Bocarsly, A. B. Mechanistic insights into C2 and C3 product generation using Ni3Al and Ni3Ga electrocatalysts for CO2 reduction. *Faraday Discuss* **2019**, 215, 192–204.
- (25) Torelli, D. A.; Francis, S. A.; Crompton, J. C.; Javier, A.; Thompson, J. R.; Brunschwig, B. S.; Soriaga, M. P.; Lewis, N. S. Nickel—Gallium-Catalyzed Electrochemical Reduction of CO2 to Highly Reduced Products at Low Overpotentials. *ACS Catal.* **2016**, *6* (3), 2100–2104.
- (26) Wang, T.; Duan, X.; Bai, R.; Li, H.; Qin, C.; Zhang, J.; Duan, Z.; Chen, K.-J.; Pan, F. Ni-Electrocatalytic CO₂ Reduction Toward Ethanol. *Adv. Mater.* **2024**, *36* (44), 2410125.
- (27) Cronin, S. P.; Dulovic, S.; Lawrence, J. A.; Filsinger, K. A.; Hernandez-Gonzalez, A. P.; Evans, R.; Stiles, J. W.; Morris, J.; Pelczer, I.; Bocarsly, A. B. Direct Synthesis of 1-Butanol with High Faradaic Efficiency from CO(2) Utilizing Cascade Catalysis at a Ni-Enhanced (Cr(2)O(3))(3)Ga(2)O(3) Electrocatalyst. J. Am. Chem. Soc. 2023, 145 (12), 6762–6772.
- (28) Yang, X.; Ding, H.; Li, S.; Zheng, S.; Li, J.-F.; Pan, F. Cation-Induced Interfacial Hydrophobic Microenvironment Promotes the C–C Coupling in Electrochemical CO2 Reduction. *J. Am. Chem. Soc.* **2024**, *146* (8), 5532–5542.
- (29) Zheng, S.; Yang, X.; Shi, Z. Z.; Ding, H.; Pan, F.; Li, J. F. The Loss of Interfacial Water-Adsorbate Hydrogen Bond Connectivity Position Surface-Active Hydrogen as a Crucial Intermediate to Enhance Nitrate Reduction Reaction. J. Am. Chem. Soc. 2024, 146 (39), 26965–26974.
- (30) Wang, Y.-H.; Zheng, S.; Yang, W.-M.; Zhou, R.-Y.; He, Q.-F.; Radjenovic, P.; Dong, J.-C.; Li, S.; Zheng, J.; Yang, Z.-L.; et al. In situ Raman spectroscopy reveals the structure and dissociation of interfacial water. *Nature* **2021**, *600* (7887), 81–85.
- (31) Le, J.-B.; Chen, A.; Kuang, Y.; Cheng, J. Molecular understanding of cation effects on double layers and their significance to CO-CO dimerization. *Natl. Sci. Rev.* **2023**, *10* (9), nwad105.
- (32) Cao, W.; Xia, G. J.; Yao, Z.; Zeng, K. H.; Qiao, Y.; Wang, Y. G. Aldehyde Hydrogenation by Pt/TiO(2) Catalyst in Aqueous Phase: Synergistic Effect of Oxygen Vacancy and Solvent Water. *JACS Au.* **2023**, *3* (1), 143–153.
- (33) Liu, X.; Jiao, Y.; Zheng, Y.; Jaroniec, M.; Qiao, S.-Z. Mechanism of C-N bonds formation in electrocatalytic urea production revealed by ab initio molecular dynamics simulation. *Nat. Commun.* **2022**, *13* (1), 5471.
- (34) Jarzynski, C. Nonequilibrium Equality for Free Energy Differences. *Phys. Rev. Lett.* **1997**, *78* (14), 2690–2693.
- (35) Woo, T. K.; Margl, P. M.; Blöchl, P. E.; Ziegler, T. A Combined Car—Parrinello QM/MM Implementation for ab Initio Molecular Dynamics Simulations of Extended Systems: Application to Transition Metal Catalysis. *J. Phys. Chem. B* **1997**, *101* (40), 7877—7880.
- (36) Vos, R. E.; Koper, M. T. M. Nickel as Electrocatalyst for CO₍₂₎ Reduction: Effect of Temperature, Potential, Partial Pressure, and Electrolyte Composition. *ACS Catal.* **2024**, *14*, 4432–4440.

- (37) Liu, S.; Li, Y.; Wang, D.; Xi, S.; Xu, H.; Wang, Y.; Li, X.; Zang, W.; Liu, W.; Su, M.; Yan, K.; et al. Alkali cation-induced cathodic corrosion in Cu electrocatalysts. *Nat. Commun.* **2024**, *15* (1), 5080.
- (38) Kim, H.; Kim, M. M.; Cho, J.; Lee, S.; Kim, D. H.; Shin, S.-J.; Utsunomiya, T.; Goddard, W. A.; Katayama, Y.; Kim, H.; et al. Cation Effect on the Electrochemical Platinum Dissolution. *J. Am. Chem. Soc.* **2025**, *147* (5), 4667–4674.
- (39) Hersbach, T. J. P.; McCrum, I. T.; Anastasiadou, D.; Wever, R.; Calle-Vallejo, F.; Koper, M. T. M. Alkali Metal Cation Effects in Structuring Pt, Rh, and Au Surfaces through Cathodic Corrosion. ACS Appl. Mater. Interfaces 2018, 10 (45), 39363–39379.
- (40) Medford, A. J.; Vojvodic, A.; Hummelshøj, J. S.; Voss, J.; Abild-Pedersen, F.; Studt, F.; Bligaard, T.; Nilsson, A.; Nørskov, J. K. From the Sabatier principle to a predictive theory of transition-metal heterogeneous catalysis. *J. Catal.* **2015**, 328, 36–42.
- (41) Vasileff, A.; Xu, C.; Jiao, Y.; Zheng, Y.; Qiao, S.-Z. Surface and Interface Engineering in Copper-Based Bimetallic Materials for Selective CO 2 Electroreduction. *Chem* **2018**, *4* (8), 1809–1831.
- (42) Koga, O.; Hori, Y. Reduction of adsorbed CO on a Ni electrode in connection with the electrochemical reduction of CO₂. *Electrochim. Acta* **1993**, 38 (10), 1391–1394.
- (43) Hori, Y.; Koga, O.; Aramata, A.; Enyo, M. Infrared Spectroscopic Observation of Adsorbed CO Intermediately Formed in the Electrochemical Reduction of CO₂ at a Nickel Electrode. *Bull. Chem. Soc. Jpn.* **1992**, *65* (11), 3008–3010.
- (44) Hori, Y.; Murata, A. Electrochemical Evidence of Intermediate Formation of Adsorbed CO in Cathodic Reduction of CO₂ at a Nickel Electrode. *Electrochim. Acta* **1990**, *35* (11–12), 1777–1780.
- (45) Yan, H.-M.; Wang, Z.-X.; Wang, Y.-M.; Xia, G.-J.; Wang, Y.-G. Fast Transformation of CO₂ into CO Via a Hydrogen Bond Network on the Cu Electrocatalysts. *J. Phys. Chem. C* **2022**, *126* (18), 7841–7848
- (46) Wang, Y.; Zhang, J.; Zhao, J.; Wei, Y.; Chen, S.; Zhao, H.; Su, Y.; Ding, S.; Xiao, C. Strong Hydrogen-Bonded Interfacial Water Inhibiting Hydrogen Evolution Kinetics to Promote Electrochemical ${\rm CO_2}$ Reduction to ${\rm C_{2+}}$. ACS Catal. 2024, 14 (5), 3457–3465.
- (47) Bligaard, T.; Nørskov, J. K.; Dahl, S.; Matthiesen, J.; Christensen, C. H.; Sehested, J. The Brønsted-Evans-Polanyi relation and the volcano curve in heterogeneous catalysis. *J. Catal.* **2004**, 224 (1), 206–217.
- (48) Xiao, H.; Cheng, T.; Goddard, W. A.; Sundararaman, R. Mechanistic Explanation of the pH Dependence and Onset Potentials for Hydrocarbon Products from Electrochemical Reduction of CO on Cu (111). *J. Am. Chem. Soc.* **2016**, *138* (2), 483–486.
- (49) Zheng, S.; Liang, X.; Pan, J.; Hu, K.; Li, S.; Pan, F. Multi-Center Cooperativity Enables Facile C–C Coupling in Electrochemical CO2 Reduction on a Ni2P Catalyst. ACS Catal. 2023, 13 (5), 2847–2856.
- (50) Garza, A. J.; Bell, A. T.; Head-Gordon, M. Mechanism of CO₂ Reduction at Copper Surfaces: Pathways to C₂ Products. ACS Catal. **2018**, 8 (2), 1490–1499.
- (51) Peterson, A. A.; Abild-Pedersen, F.; Studt, F.; Rossmeisl, J.; Nørskov, J. K. How copper catalyzes the electroreduction of carbon dioxide into hydrocarbon fuels. *Energy Environ. Sci.* **2010**, 3 (9), 1311.
- (52) Ding, H.; Zheng, S.; Yang, X.; Pan, J.; Chen, Z.; Zhang, M.; Li, S.; Pan, F. Role of Surface Hydrogen Coverage in C–C Coupling Process for CO2 Electroreduction on Ni-Based Catalysts. *ACS Catal.* **2024**, *14* (19), 14330–14338.
- (53) Li, H.; Li, X.; Wang, P.; Zhang, Z.; Davey, K.; Shi, J. Q.; Qiao, S. Z. Machine Learning Big Data Set Analysis Reveals C-C Electro-Coupling Mechanism. J. Am. Chem. Soc. 2024, 146 (32), 22850–22858
- (54) Kristoffersen, H. H.; Chan, K. Towards constant potential modeling of CO-CO coupling at liquid water-Cu(1 0 0) interfaces. *J. Catal.* **2021**, 396, 251–260.
- (55) Sandberg, R. B.; Montoya, J. H.; Chan, K.; Nørskov, J. K. CO-CO coupling on Cu facets: Coverage, strain and field effects. *Surf. Sci.* **2016**, *654*, 56–62.

- (56) Qin, X.; Hansen, H. A.; Honkala, K.; Melander, M. M. Cation-induced changes in the inner- and outer-sphere mechanisms of electrocatalytic CO₂ reduction. *Nat. Commun.* **2023**, *14* (1), 7607.
- (57) Li, Y.; Zheng, S.; Liu, H.; Xiong, Q.; Yi, H.; Yang, H.; Mei, Z.; Zhao, Q.; Yin, Z.-W.; Huang, M.; Lin, Y.; et al. Sequential coreduction of nitrate and carbon dioxide enables selective urea electrosynthesis. *Nat. Commun.* **2024**, *15* (1), 176.
- (58) Zheng, S.; Ding, H.; Yang, X.; Li, S.; Pan, F. Automating Discovery of Electrochemical Urea Synthesis Reaction Paths via Active Learning and Graph Theory. CCS Chem. 2024, 1–13.
- (59) Pan, J.; Ding, H.; Yang, X.; Liang, X.; Wu, S.; Zhang, M.; Li, S.; Zheng, S.; Pan, F. Autonomous Exploitation of Reaction Pathways for Electrochemical C—N Coupling on Single-Atom Catalysts. *ACS Catal.* **2025**, *15*, 457–467.
- (60) Lin, W.-Y.; Chen, Z.-X.; Xiong, H.; Li, H.-C.; Ho, Y.-S.; Hsieh, C.-T.; Lu, Q.; Cheng, M.-J. Identification of CO₂ as a Reactive Reagent for C–C Bond Formation via Copper-Catalyzed Electrochemical Reduction. *ACS Catal.* **2023**, *13* (17), 11697–11710.
- (61) Preikschas, P.; Zhang, J.; Seemakurthi, R. R.; Lian, Z.; Martín, A. J.; Xi, S.; Krumeich, F.; Ma, H.; Zhou, Y.; López, N.; Yeo, B. S.; et al. CO₂ Electroreduction to Long-Chain Hydrocarbons on Cobalt Catalysts. *Adv. Energy Mater.* **2024**, *14* (47), 2401447.
- (62) Gao, D.; Zhou, H.; Cai, F.; Wang, J.; Wang, G.; Bao, X. Pd-Containing Nanostructures for Electrochemical CO₂ Reduction Reaction. ACS Catal. 2018, 8 (2), 1510–1519.
- (63) Ji, L.; Li, L.; Ji, X.; Zhang, Y.; Mou, S.; Wu, T.; Liu, Q.; Li, B.; Zhu, X.; Luo, Y.; et al. Highly Selective Electrochemical Reduction of CO₂ to Alcohols on an FeP Nanoarray. *Angew. Chem., Int. Ed.* **2020**, 59 (2), 758–762.
- (64) Kortlever, R.; Peters, I.; Balemans, C.; Kas, R.; Kwon, Y.; Mul, G.; Koper, M. T. Palladium-gold catalyst for the electrochemical reduction of CO_2 to C_1 - C_5 hydrocarbons. *Chem. Commun.* **2016**, 52 (67), 10229–10232.
- (65) Calvinho, K. U. D.; Alherz, A. W.; Yap, K. M. K.; Laursen, A. B.; Hwang, S.; Bare, Z. J. L.; Clifford, Z.; Musgrave, C. B.; Dismukes, G. C. Surface Hydrides on Fe₂P Electrocatalyst Reduce CO₂ at Low Overpotential: Steering Selectivity to Ethylene Glycol. *J. Am. Chem. Soc.* **2021**, *143* (50), 21275–21285.
- (66) Zhong, M.; Tran, K.; Min, Y.; Wang, C.; Wang, Z.; Dinh, C. T.; De Luna, P.; Yu, Z.; Rasouli, A. S.; Brodersen, P.; et al. Accelerated discovery of CO2 electrocatalysts using active machine learning. *Nature* **2020**, *581* (7807), 178–183.
- (67) Li, P.; Bi, J.; Liu, J.; Wang, Y.; Kang, X.; Sun, X.; Zhang, J.; Liu, Z.; Zhu, Q.; Han, B. p-d Orbital Hybridization Induced by p-Block Metal-Doped Cu Promotes the Formation of C(2+) Products in Ampere-Level CO(2) Electroreduction. *J. Am. Chem. Soc.* **2023**, *145* (8), 4675–4682.
- (68) Du, Z.-Y.; Li, S.-B.; Liang, G.-H.; Xie, Y.-M.; A, Y.-L.; Zhang, Y.; Zhang, H.; Tian, J.-H.; Zheng, S.; Zheng, Q.-N.; et al. Promoting Water Activation via Molecular Engineering Enables Efficient Asymmetric C–C Coupling during CO2 Electroreduction. *J. Am. Chem. Soc.* **2024**, 146 (47), 32870–32879.
- (69) Wang, M.; Zhang, G.; Wang, H.; Wang, Z.; Zhou, Y.; Nie, X.; Yin, B. H.; Song, C.; Guo, X. Understanding and Tuning the Effects of H(2)O on Catalytic CO and CO(2) Hydrogenation. *Chem. Rev.* **2024**, 124 (21), 12006–12085.
- (70) Demuth, J. E.; Marcus, P. M.; Jepsen, D. W. Analysis of low-energy-electron-diffraction intensity spectra for (001), (110), and (111) nickel. *Phys. Rev. B* **1975**, *11* (4), 1460–1474.
- (71) Torelli, D. A.; Francis, S. A.; Crompton, J. C.; Javier, A.; Thompson, J. R.; Brunschwig, B. S.; Soriaga, M. P.; Lewis, N. S. Nickel–Gallium–Catalyzed Electrochemical Reduction of CO₂ to Highly Reduced Products at Low Overpotentials. *ACS Catal.* **2016**, *6* (3), 2100–2104.
- (72) Paris, A. R.; Bocarsly, A. B. Ni–Al Films on Glassy Carbon Electrodes Generate an Array of Oxygenated Organics from CO₂. ACS Catal. **2017**, 7 (10), 6815–6820.
- (73) Zhao, Q.; Martirez, J. M. P.; Carter, E. A. Charting C-C coupling pathways in electrochemical CO ₂ reduction on Cu(111)

- using embedded correlated wavefunction theory. *Proc. Natl. Acad. Sci. U. S. A.* **2022**, *119* (44), No. e2202931119.
- (74) Kresse, G.; Hafner, J. Ab initio molecular dynamics for liquid metals. *Phys. Rev. B* **1993**, 47 (1), 558–561.
- (75) Kresse, G.; Furthmuller, J. Efficient iterative schemes for ab initio total-energy calculations using a plane-wave basis set. *Phys. Rev.* B **1996**, 54 (16), 11169–11186.
- (76) Blöchl, P. E. Projector augmented-wave method. *Phys. Rev. B* **1994**, *50* (24), 17953–17979.
- (77) Perdew, J. P.; Burke, K.; Ernzerhof, M. Generalized Gradient Approximation Made Simple. *Phys. Rev. Lett.* **1996**, 77 (18), 3865–3868
- (78) Grimme, S.; Antony, J.; Ehrlich, S.; Krieg, H. A consistent and accurate ab initio parametrization of density functional dispersion correction (DFT-D) for the 94 elements H-Pu. *J. Chem. Phys.* **2010**, 132 (15), 154104.
- (79) Dronskowski, R.; Bloechl, P. E. Crystal orbital Hamilton populations (COHP): energy-resolved visualization of chemical bonding in solids based on density-functional calculations. *J. Phys. Chem.* **1993**, 97 (33), 8617–8624.
- (80) Maintz, S.; Deringer, V. L.; Tchougréeff, A. L.; Dronskowski, R. LOBSTER: A tool to extract chemical bonding from plane-wave based DFT. *J. Comput. Chem.* **2016**, *37* (11), 1030–1035.

